The Pre-He White Dwarf in the Post-mass Transfer Binary EL CVn

Luqian Wang (王璐茜)[1] , Douglas R. Gies[1] , Kathryn V. Lester[1] , Zhao Guo[2] , Rachel A. Matson[3] , Geraldine J. Peters[4],
Vik S. Dhillon[5,6], Tim Butterley[7], Stuart P. Littlefair[5] , Richard W. Wilson[7], and Pierre F. L. Maxted[8]

[1] Center for High Angular Resolution Astronomy and Department of Physics and Astronomy, Georgia State University, P.O. Box 5060, Atlanta, GA 30302-5060, USA; lwang@chara.gsu.edu, gies@chara.gsu.edu, lester@astro.gsu.edu

[2] Center for Exoplanets and Habitable Worlds, Department of Astronomy and Astrophysics, 525 Davey Laboratory, Pennsylvania State University, University Park, PA 16802, USA; zxg124@psu.edu

[3] NASA Ames Research Center, Moffett Field, CA 94035, USA; rachel.a.matson@nasa.gov

[4] Space Sciences Center, Department of Physics and Astronomy, University of Southern California, Los Angeles, CA 90089-1341, USA; gpeters@usc.edu

[5] Department of Physics and Astronomy, University of Sheffield, Sheffield S3 7RH, UK; vik.dhillon@sheffield.ac.uk, s.littlefair@shef.ac.uk

[6] Instituto de Astrofísica de Canarias, E-38205, La Laguna, Tenerife, Spain

[7] Department of Physics, Durham University, South Road, Durham, DH1 3LE, UK; timothy.butterley@durham.ac.uk, r.w.wilson@durham.ac.uk

[8] Astrophysics Group, Keele University, Staffordshire, ST5 5BG, UK; p.maxted@keele.ac.uk

Abstract

EL CVn is the prototype of a class of eclipsing binaries that consist of an A- or F-type main-sequence star and a hot, low-mass, pre-He white dwarf (pre-He WD), the stripped down remains of the former mass donor. Here we present the first direct detection and characterization of the spectrum of the pre-He WD in EL CVn that was made possible through far-UV spectroscopy with the *Hubble Space Telescope* Cosmic Origins Spectrograph. These spectra straddle the wavelength range where flux dominance shifts from the pre-He WD to the A star. Radial velocities of both components were measured from the far-UV spectra and new optical spectra from the Apache Point Observatory Astrophysical Research Consortium Echelle Spectrograph. We also obtained fast cadence photometry of the eclipses with the pt5m telescope at the Roque de los Muchachos Observatory. A combined analysis of the velocities and light curve yields the component masses and radii. We applied a Doppler tomography algorithm to reconstruct the individual spectra, and we compared these to models to estimate the effective temperatures. The pre-He WD has low mass ($0.176 \pm 0.004\,M_\odot$), is small ($0.284 \pm 0.003\,R_\odot$), and is relatively hot ($11{,}800 \pm 400$ K), and these parameters are approximately consistent with predictions for a star stripped through stable mass transfer. The spectral lines of the pre-He WD show that its atmosphere is H-rich, He-depleted, and metal-poor, probably as the result of elemental diffusion that has occurred since mass transfer ceased.

Unified Astronomy Thesaurus concepts: Stellar evolution (1599); Eclipsing binary stars (444); White dwarf stars (1799)

1. Introduction

Over the last few years photometric surveys have revealed a class of post-mass transfer binaries that consist of a main-sequence (MS) star and a hotter, smaller companion stripped of its H envelope. One of the first discoveries was made by Maxted et al. (2011) though the Wide Angle Search for Planets (WASP) photometric survey. They found that WASP 0247−25 displays a total eclipse of a small, hot star by a MS A-type star. Photometry and spectroscopy revealed that the hot companion is a precursor to a low mass, He core, white dwarf (pre-He WD). Maxted et al. (2014) expanded the search through WASP and found another 17 similar eclipsing binaries with orbital periods between 0.7 and 2.2 days and with MS components with effective temperatures of 8800–15,000 K. EL CVn is the brightest star in the sample ($V = 9.4$), and it is the prototype of eclipsing binaries that consists of an A/F-type MS star and a low-mass pre-He WD. The orbital period of EL CVn is 0.7956 days, and the brighter component has a spectral classification of A3 V (Maxted et al. 2014). The *Kepler* survey yielded another 13 EL CVn-type systems, including KOI-74 (van Kerkwijk et al. 2010; Bloemen et al. 2012), KIC-10657664 (Carter et al. 2011), KOI-1224 (Breton et al. 2012), KIC-9164561, KOI-10727668 (Rappaport et al. 2015), KIC-4169521, KOI-3818, KIC-2851474, KIC-9285587 (Faigler et al. 2015), KOI-81 (Matson et al. 2015), KIC-8262223 (Guo et al. 2017), KIC-8087799, and KIC-10989032

(Zhang et al. 2017). The pre-He WD stars in the *Kepler* sample have orbital periods of 0.9–23.9 days, radii of 0.03–1.3 $R_\odot$, and effective temperatures of 7119–19,400 K. Wang et al. (2018) obtained photometry and spectroscopy of V1224 Cas and concluded that it is an EL CVn-type binary consisting of a pre-He WD and a MS companion displaying δ Scuti-type pulsations. They reported that the pre-He component has an orbital period of 2.3 days, radius of 0.97 $R_\odot$, and effective temperature of 9516 K. van Roestel et al. (2018) used supervised machine learning methods to search light curves (LCs) from the Palomar Transient Factory, and they discovered 36 new EL CVn-type binaries. The radius and effective temperature ranges of these newly discovered pre-He WD companions are 0.3–0.7 $R_\odot$ and 8000–17,000 K, respectively. Recently, Masuda et al. (2019) conducted a photometric and spectroscopic analysis of a self-lensing binary KIC-8145411. They concluded that the low-mass WD companion has a mass of 0.2 $M_\odot$ and a long orbital period of 455.8 days.

The two main formation scenarios proposed for the EL CVn-type binaries are stable Roche-lobe overflow (RLOF) and unstable, rapid, common envelope evolution (CE). Based on calculations of binary evolution, Chen et al. (2017) argued that EL CVn-type binaries are likely formed from the stable mass transfer process instead of the CE one, because the latter generally leads to a merger of the components. The stable mass transfer scenario starts with two MS stars, and the more

massive star evolves away from the MS to become a red giant star. The system experiences RLOF as the massive donor star starts to transfer mass and angular momentum to the low-mass gainer star. This process continues until the mass donor star loses its outer envelope and becomes a stripped red giant core (Maxted et al. 2011). Because it is not massive enough to ignite helium burning, the star undergoes H shell burning at nearly constant luminosity. After hydrogen consumption, the star will eventually fade to become a He WD. Chen et al. (2017) applied the MESA binary evolution sequences and performed a Monte Carlo simulation for binary population synthesis. They estimated that EL CVn-type binaries with an orbital period of $P \leqslant 2.2$ days comprise a population of about $2–5 \times 10^6$ in the Galaxy. The EL CVn-type binaries discovered thus far represent a small portion of the population in the local galactic environment, so a large fraction remain to be discovered in future photometric surveys. It is crucial to determine the physical properties of this type of binary system as tests to trace their evolutionary paths in the H-R diagram.

The challenge is to measure the spectral features of the pre-He WD directly in order to determine the orbital velocities and hence masses. Because the pre-He WD components are hotter, their spectral contribution will be larger in the UV part of the spectrum, and the only detection so far was made through UV spectroscopy of KOI-81 by Matson et al. (2015). Here we present such a UV study that has revealed the pre-He WD component in the prototype system EL CVn. We describe different sets of observations and their reduction procedures in Section 2, and analyses of the orbital radial velocity and LCs are presented in Sections 3 and 4, respectively. The orbital elements and masses are reviewed in Section 5, and the physical parameters derived from Doppler tomography reconstructions of the component spectra are discussed in Section 6. We consider the current evolutionary stage of the binary in Section 7, and summarize our findings in Section 8.

2. Observations and Data Reduction

We used three sets of observations to investigate the stellar features of EL CVn. These include far-UV (FUV) spectroscopic obervations from the *Hubble Space Telescope* (*HST*), optical spectra from the Apache Point Observatory (APO), and optical LCs from the Roque de los Muchachos Observatory at La Palma. Details of each data set follow.

2.1. FUV HST/COS Spectroscopy

We obtained the FUV spectra with *HST* using the Cosmic Origins Spectrograph (COS; Green et al. 2012). The spectra were made with the G160M grating that records the wavelength range 1405–1775 Å with a resolving power of 16,000–21,000. The spectrum is imaged onto two detector segments, B and A, with a gap of 21 Å between them. Four visits were executed between 2016 November 25 and December 1, and two observations were obtained each visit for central wavelengths of 1577 and 1600 Å. Each observation contained four subexposures with a total exposure time of 612 s. The FUV spectra were reduced and the observed flux and wavelength were calibrated using the standard COS pipeline from Fischer (2019). We used the IDL program coadd_x1d.pro from Danforth et al. (2010) to combine the four subexposures of every observation into a single spectrum in the barycentric frame. These spectra were subsequently transformed onto a uniform wavelength grid in $\log \lambda$ steps equivalent to 9.37 and 7.89 km s^{-1} pixel^{-1} for segments B and A, respectively. We did not attempt to remove any weak interstellar medium lines from the spectra. We formed matrices of all eight spectra (as functions of wavelength and time of observation) as separate data structures for the short wavelength (B) and long wavelength (A) ranges. We kept two versions of the spectra. The first set was rectified to a unit continuum by division of a spline fit of the relatively line-free regions. These rectified spectra were used to compute the radial velocities (Section 3). The second set was saved as absolute flux spectra, and these were used for reconstruction of the individual components and fitting the composite spectral energy distribution (Section 6).

2.2. Optical APO/ARCES Spectroscopy

We obtained eight optical spectra with the APO 3.5 m telescope and ARC Echelle Spectrograph (ARCES). These were made between 2017 February 16 and 2018 April 4. The ARCES instrument records the spectrum over the wavelength range of 3200–10000 Å on a 2048 × 2048 SITe CCD (Wang et al. 2003). These data have a spectral resolving power of $R \sim 31500$. We reduced the spectra following the standard IRAF procedures including cosmic-ray removal, bias subtraction, flat fielding, aperture extraction and normalization, scattered light correction, wavelength calibration line identification, dispersion correction, and heliocentric correction. We transformed the spectra from each echelle order onto a logarithmic wavelength grid with a step size of 3.92 km s^{-1} per pixel. We adopted the technique from Kolbas et al. (2015) to remove the residuals of the blaze function appearing in the spectra. The final spectra were rectified to a unit continuum and collected into a flux matrix as a function of wavelength and time of observation.

2.3. Optical pt5M LCs

We obtained two optical LCs from the 0.5 m robotic telescope (pt5m) located on the roof of the 4.2 m William Herschel Telescope building at the Roque de los Muchachos Observatory, La Palma (Hardy et al. 2015). The CCD has format of 2184 × 1472 pixels with a plate scale of 0.28 arcsec per pixel. The observations were made on the nights of 2013 May 5 and 15 using a Johnson *I*-band filter, and each observation lasted for a duration of about 4 hr with individual exposure times of 20 s and with 5 s of dead time between each exposure. These measurements recorded both of the mutual eclipses of the components. The pt5m data were reduced using the ULTRACAM pipeline software (Dhillon et al. 2007). The science frames were bias and dark subtracted, and then divided by a flat field obtained from images of a blank region of the twilight sky. Aperture photometry was then used to determine the total counts from the target and comparison stars, with the sky level estimated from an annulus surrounding each target aperture. The final result is a time series of relative magnitude as a function of heliocentric Julian date. The typical uncertainty on an individual measurement is 0.005 mag.

3. Radial Velocity Measurements

Based upon preliminary temperature estimates of the stars from Maxted et al. (2014), we expected that the short wavelength segment of the *HST*/COS spectra would be
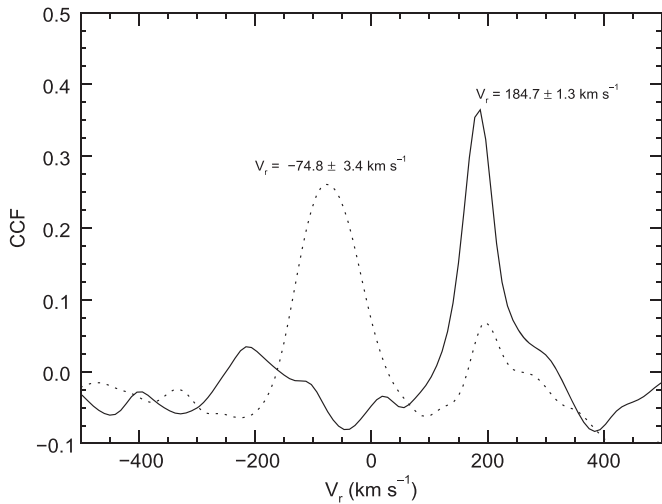
Figure 1. Plot of cross-correlation functions of EL CVn for each component from the *HST*/COS spectrum observed on HJD 2457717.5985. The CCF of the pre-He WD (A-star) component is plotted as a solid (dotted) line.

dominated by the flux of the hotter pre-He WD, and indeed we found that the spectral lines in that region resembled those of a late B-type star. On the other hand, the flux in the long wavelength segment of the *HST*/COS spectra is progressively more dominated by the light of the A star. Consequently, we measured radial velocities for the pre-He WD star using only the short wavelength segment and those for the A star using only the long wavelength segment.

We calculated the radial velocities using a cross-correlation function (CCF) algorithm described by Wang et al. (2017). We constructed individual model template spectra of both components using the UVBLUE grid of model fluxes that is based on Kurucz radiative transfer codes ATLAS9 and SYNTHE (Rodríguez-Merino et al. 2005). We adopted preliminary parameters of $T_{\rm eff} = 8250\,{\rm K}$ and $12{,}000\,{\rm K}$ and $\log g = 4.0$ and 4.8 for the model spectra of the A star and pre-He WD star, respectively. These model spectra are based upon solar abundances and a microturbulent velocity of $2\,{\rm km\,s^{-1}}$. The model templates were rectified to a unit continuum in the same way as the *HST*/COS spectra, transformed onto the same $\log \lambda$ wavelength grid, and smoothed according to the observed instrumental broadening. We then cross-correlated each observed spectrum of EL CVn with the model template spectrum, restricting the calculation to 1646–1743 Å and 1429–1502 Å for the A star and pre-He WD star spectra, respectively. We measured the Doppler shifts of each stellar component from the location of the CCF maximum. The radial velocity uncertainties were calculated based upon the maximum likelihood method of Zucker (2003), which depends upon the CCF peak height, second derivative at the peak location, and number of wavelength points included. The CCFs for each component for the spectrum observed on HJD 2457717.5985 are shown in Figure 1 as an example of the procedure. The radial velocity measurements V_r and their associated uncertainties σ are collected in Table 1.

We also measured the radial velocities of both components using the optical spectra from APO. We formed a model spectrum of the A star using the library of theoretical stellar spectra BLUERED from Bertone et al. (2008). We adopted the same parameters as adopted in the UV template spectra construction, and rectified and rebinned the spectrum in the

same way as done with the ARCES spectra, and smoothed the model to the observed instrumental broadening. Most of the echelle orders contain very weak metallic lines or very broad H-Balmer lines that are difficult to measure. In the end, we restricted the CCF measurements for the A star to two echelle orders that contained the strong Ca I $\lambda4226$ and Mg II $\lambda4481$ lines.

We inspected the ARCES spectra and found that the only obvious line feature associated with the pre-He WD star is the Mg II $\lambda4481$ profile that displays the Doppler shifted components of both stars. We measured the line centroid of the component of the pre-He WD star in only those spectra with large velocity shifts where it was cleanly separated from the line component of the A star.

The radial velocities from *HST*/COS and APO/ARCES probably have systematic offsets because of the differences in spectral regions and measurement methods. Consequently, we made preliminary orbital velocity fits of each group separately in order to estimate any systematic offsets. We computed the circular orbital solution using the nonlinear, least-squares technique from Morbey & Brosterhus (1974) by fixing the orbital period, P, epoch of inferior conjunction of the A star, T_0 (equal to the epoch of the LC deeper eclipse; see Section 5), and semiamplitude, K, and then solving for the systemic velocity, γ, alone. These estimates of systemic velocity are collected in Table 2 which includes a fit of 15 radial velocity measurements of the A star from Maxted et al. (2014). The difference of derived systemic velocity for the A star from that for *HST*/COS led to offsets of $\Delta\gamma = -0.35\,{\rm km\,s^{-1}}$ for the APO/ARCES measurements and $\Delta\gamma = +11.43\,{\rm km\,s^{-1}}$ for the Maxted et al. (2014) published measurements. Likewise, the difference of derived systemic velocity for the pre-He WD star from the APO/ARCES radial velocities led to an offset of $\Delta\gamma = +2.93\,{\rm km\,s^{-1}}$ from the *HST*/COS measurements. These offsets were added to the APO/ARCES velocities to place them in the same reference frame as the *HST*/COS measurements, which have smaller radial velocity uncertainties (Table 1). Table 1 lists the component (P for the A star and S for the pre-He WD star), HJD of mid-exposure, orbital phase (Section 5), offset-corrected radial velocity, its uncertainty, the observed minus calculated $(O - C)$ residual, and the observation source.

The final circular orbital elements were derived with fixed P and T_0 (Section 5) by fitting all the available data in the *HST*/COS reference frame. The derived values of K and γ are presented for both stars in Table 2 along with the mass products and projected semimajor axis. The final two rows give the standard deviations of the fits, which are comparable to the measurement uncertainties. The radial velocities and orbital velocity curves are shown in Figure 2. Note that the measured semiamplitude of the A star, K_1, was not corrected for the effects of irradiation by the pre-He WD, because any such effects are negligible given the low luminosity of the pre-He WD, the comparable temperatures of the stars, and the lack of evidence of irradiation in the LC (Maxted et al. 2014). We also derived the eccentric orbital elements from the radial velocities using the eccentricity e and the longitude of periastron ω estimated from the LC (Section 4), and we noticed that the fitted semiamplitudes for both components were the same within errors between the circular and the eccentric orbital fits. Consequently, we report in Table 2 only the results from the adopted circular fit.

Table 1
Radial Velocity Measurements of EL CVn

Primary/ Secondary	Date (HJD-2400000)	Orbital Phase	V_r[a] (km s^{-1})	σ (km s^{-1})	$(O-C)$ (km s^{-1})	Observation Source
P	57717.5985	0.7581	−74.84	3.40	1.68	HST/COS
P	57717.6148	0.7786	−74.93	3.64	1.16	HST/COS
P	57722.6693	0.1314	−28.70	3.14	−2.48	HST/COS
P	57722.7172	0.1917	−24.97	3.28	−4.51	HST/COS
P	57722.7900	0.2832	−15.98	3.47	3.18	HST/COS
P	57722.8526	0.3618	−29.56	2.98	−4.15	HST/COS
P	57723.8658	0.6353	−64.28	3.00	5.06	HST/COS
P	57723.9313	0.7176	−73.68	3.38	2.28	HST/COS
P	57800.9918	0.5726	−59.26	4.02	1.07	APO/ARCES
P	57801.0082	0.5932	−59.71	3.56	3.88	APO/ARCES
P	57821.7924	0.7163	−74.70	4.14	1.21	APO/ARCES
P	58089.9927	0.8091	−78.59	3.03	−4.01	APO/ARCES
P	58090.0258	0.8507	−72.49	2.63	−1.55	APO/ARCES
P	58146.9719	0.4246	−30.55	3.29	3.76	APO/ARCES
P	58147.0108	0.4735	−39.81	2.42	2.92	APO/ARCES
P	58212.7782	0.1345	−25.75	2.53	0.09	APO/ARCES
S	57717.5985	0.7581	184.72	1.25	−1.45	HST/COS
S	57717.6148	0.7786	184.95	1.21	2.27	HST/COS
S	57722.6693	0.1314	−220.18	1.51	3.20	HST/COS
S	57722.7172	0.1917	−269.97	1.26	0.27	HST/COS
S	57722.7900	0.2832	−284.54	1.24	−3.70	HST/COS
S	57722.8526	0.3618	−227.24	1.24	2.75	HST/COS
S	57723.8658	0.6353	122.28	1.34	−5.46	HST/COS
S	57723.9313	0.7176	181.10	1.23	−0.51	HST/COS
S	57821.7924	0.7163	186.06	2.07	4.86	APO/ARCES
S	58089.9927	0.8091	168.54	5.42	−1.82	APO/ARCES
S	58090.0258	0.8507	144.70	1.91	3.98	APO/ARCES
S	58212.7782	0.1345	−228.10	2.08	−1.65	APO/ARCES

Note.
[a] Offsets of $\Delta\gamma = -0.35$ km s^{-1} and $\Delta\gamma = +2.93$ km s^{-1} were added to the APO/ARCES measurements for the A star (P) and pre-He WD (S), respectively, to place them in the HST/COS reference frame (see Section 3).

Table 2
Orbital Elements of EL CVn

Element	Value
P (days)	$0.79562735 \pm 0.00000014$
T_{conj} (HJD-2400000)	56418.5315 ± 0.0003
K_1 (km s^{-1})	29.01 ± 0.41
K_2 (km s^{-1})	236.21 ± 1.06
γ_1[HST] (km s^{-1})	-47.36 ± 1.05
γ_1[APO] (km s^{-1})	-47.01 ± 1.25
γ_1[Maxted] (km s^{-1})	-58.79 ± 0.67
γ_1[Merged] (km s^{-1})	-47.55 ± 0.33
γ_2 [HST] (km s^{-1})	-49.86 ± 1.12
γ_2 [APO] (km s^{-1})	-52.79 ± 2.52
γ_2 [Merged] (km s^{-1})	-49.73 ± 0.95
M_2/M_1	0.1228 ± 0.0018
$a \sin i$ ($R_\odot$)	4.169 ± 0.018
$M_1 \sin^3 i$ ($M_\odot$)	1.370 ± 0.013
$M_2 \sin^3 i$ ($M_\odot$)	0.168 ± 0.003
σ_1 (km s^{-1})	1.8
σ_2 (km s^{-1})	3.3

Figure 2. Radial velocity curve of EL CVn. In the top panel, the blue dots represent measurements from HST, green dots the measurements from APO, and published data from Maxted et al. (2014) appear as orchid dots. The errors of the radial velocity measurements are smaller than the dots, and are thus not shown in the top panel. The bottom panel displays the difference between observed and calculated velocities, and the measurement errors are portrayed here. Orbital phase $\phi = 0.0$ is the epoch when the A-type star reaches inferior conjunction.

4. LC Fit

Maxted et al. (2014) performed an LC analysis of EL CVn photometry from the WASP survey, and they reported orbital parameters from fits with the JKTEBOP modeling code. We
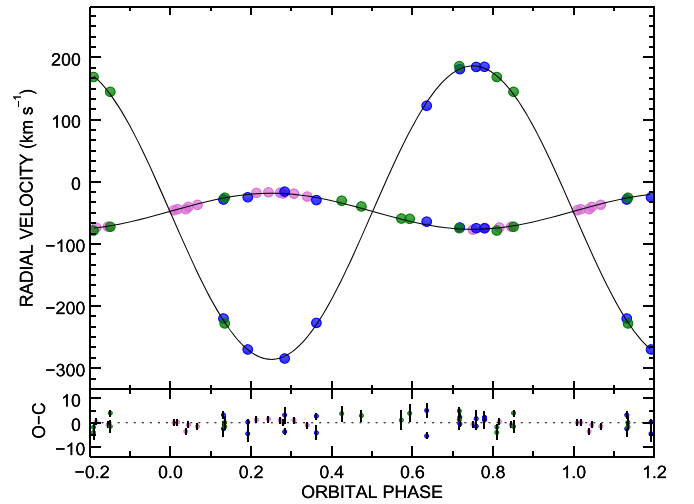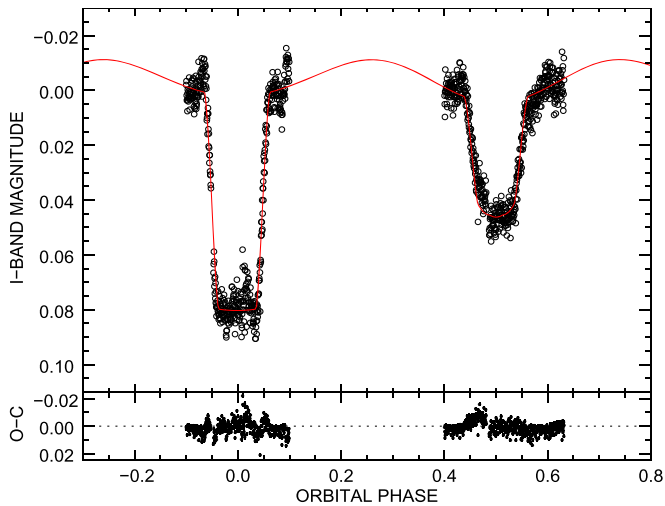
Figure 3. Top panel shows the LC of EL CVn observed on the nights of 2013 May 5 and 15, and the ELC model fit is shown as a red solid line. The bottom panel displays the residuals between the observed and model LCs.

applied the eclipsing light curve (ELC) code from Orosz & Hauschildt (2000) to make fits of the two eclipse observations made on 2013 May 5 and 2013 May 15 from the pt5m telescope (Section 2.3) that are illustrated in Figure 3. This photometry covers only the eclipse phases, so we are missing the phases between eclipses that show evidence of the tidal deformation of the A star (see Figure A1 in Maxted et al. 2014). On the other hand, the pt5m photometry has approximately nine times faster cadence than the WASP photometry, so the new results are useful for a reanalysis of fitting parameters sensitive to details of the eclipses.

We set most of the fitting parameters at the outset based upon the spectroscopic results including the semiamplitudes, mass ratio, and orbital period (Table 2). We explored solutions for a range of stellar temperature, but in the end we set the temperatures to the averages from spectroscopy (Table 4) that differed insignificantly from the optimal fits. These temperatures (and gravities) then set the adopted specific intensities in the I band from model atmospheres (Orosz & Hauschildt 2000). Two other parameters were fixed at values determined by the WASP LC fits by Maxted et al. (2014), because tests showed that they produced optimal fits. These parameters are the A-star fractional radius, $R_1/a = 0.346 \pm 0.012$, and the orbital inclination, $i = 80°.3 \pm 1°.8$. We then solved for four other parameters that each change the LC in a different way, so that we could find a χ^2 minimum in each case that led to a unique best fit. The first parameter is T_{conj}, the epoch of A-star inferior conjunction (equal to the mid-point of the deeper eclipse), and the result is listed in Table 3. We noticed that the two eclipses are not exactly separated by half of the orbital period, which indicates that the orbit has a non-zero eccentricity. We thus used the phase difference between eclipses (sensitive to $e \cos \omega$) and the difference in the eclipse durations (sensitive to $e \sin \omega$) to optimize the fit (see appendices in Matson et al. 2016). The results are $e \cos \omega = 0.0019 \pm 0.0005$ and $e \sin \omega = -0.0149 \pm 0.0086$. The durations of eclipse ingress and egress are sensitive to the fractional radius of the pre-He WD, and the fits yield an estimate of $R_2/a = 0.0671 \pm 0.0006$. The uncertainties in the parameters were set by the range where the normalized, reduced χ_ν^2 increased to $1 + 1/\nu$, where ν is

the number of degrees of freedom. For our purposes, we used $\nu = N_{eff} - 1$, where $N_{eff} = 252$ is the number of measurements in the ingress and egress parts of the LC that are critical for these specific parameters. The uncertainty in the fractional radius R_2/a includes a systematic factor for the finite exposure time.

The final ELC model LC based on these optimized parameters is shown in Figure 3. The derived parameters are the same within errors as those found by Maxted et al. (2014), and the residuals from the fit are generally within the expected scatter ($\pm 3\sigma$). However, there is an asymmetric feature in the secondary eclipse that appears slightly brighter than expected prior to minimum. The ELC model is axially symmetric, so such features cannot be fit without adding parameters for spatial features in the photosphere of the A star. Additional photometry will be required to confirm this residual feature in the LC.

5. Orbital Elements, Masses, and Radii

We determined the orbital period by combining estimates of orbital epoch from published and our own values. For consistency, we define the zero phase as the epoch T_{conj} when the primary A-type star reaches inferior conjunction. This phase reference is adopted throughout this work. The different sources of orbital epoch are collected in Table 3, which includes photometry from *Hipparcos* (Otero & Dubovsky 2004), WASP (Maxted et al. 2014), and pt5m (Section 4). We also include estimates from fits of subsets of the radial velocity measurements including those for the A star from McDonald Observatory spectra (Maxted et al. 2014) and from *HST*/COS and APO/ARCES spectra (Section 3) plus those for the pre-He WD from *HST*/COS and APO/ARCES (Section 3). We calculated the number of orbits elapsed relative to T_{conj} from the pt5m photometry (column 3 of Table 3), and then we made a least-squares, linear fit of epoch as a function of orbit number (see Figure 4). The derived slope and intercept yield the orbital period and global epoch, respectively (given in the first two rows of Table 2). The observed minus calculated ($O - C$) epoch times are listed in column 4 of Table 3, and these are generally comparable to the uncertainties in the individual determinations of epoch (larger for the radial velocity sets). We adopted these P and T_{conj} values in the final iteration of the radial velocity orbital fit given in Table 2.

The inclination-dependent quantities in Table 2 are transformed to binary parameters by the adopting the orbital inclination $i = 80°.3 \pm 1°.8$ derived from the fit of the LC by Maxted et al. (2014). Table 4 lists estimates for the semimajor axis a and the individual masses M_1 and M_2. Next, the fractional radii from the LC fits (R_1/a from Maxted et al. 2014; R_2/a from Section 4) are multiplied by a to find the physical radii R_1 and R_2. We find that both stars are well within their Roche radii, 2.4 $R_\odot$ and 0.9 $R_\odot$ for the A star and pre-He WD, respectively, despite the small dimensions of the orbit. Table 4 also lists the gravitational acceleration $\log g$ derived from M and R. Finally, we estimate the stellar angular diameters θ from the ratio of the radius and distance, which is given as 264.4 ± 2.5 pc from the Gaia DR2 results (Bailer-Jones et al. 2018). We will use these θ estimates in the next section to help estimate the stellar effective temperatures.

5

Table 3
Epochs of A-star Inferior Conjunction

Data Source	T_{conj} (HJD-2400000)	Orbit Number	$O - C$ (10^{-3} days)	Reference Source
Hipparcos photometry	48331.7780 ± 0.0020	−10164	2.9	Otero & Dubovsky (2004)
WASP photometry	54230.5558 ± 0.0005	−2750	−0.4	Maxted et al. (2014)
McDonald $V_r(1)$[a]	55931.6128 ± 0.0031	−612	5.3	Maxted et al. (2014)
pt5m photometry	56418.5313 ± 0.0004	0	−0.2	This work
COS and APO $V_r(1)$[a]	57723.3731 ± 0.0047	1640	12.8	This work
COS and APO $V_r(2)$[b]	57822.0195 ± 0.0012	1764	1.4	This work

Notes.
[a] (1) is the subset of radial velocity measurements for the A star.
[b] (2) is the subset of radial velocity measurements for the pre-He WD.
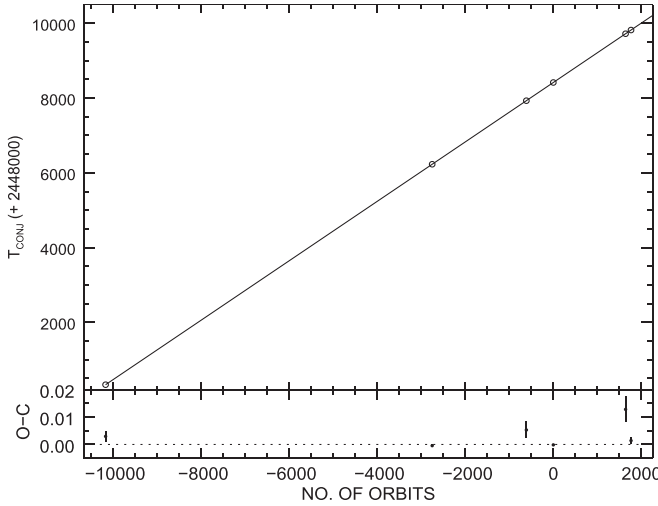
Figure 4. Top panel plots the epoch and orbit number of each data set in Table 3 and the corresponding, least-squares linear fit. The derived slope (i.e., the orbital period) and intercept (global epoch) are listed in Table 2. The bottom panel displays the differences between the observed epochs and the fit.

Table 4
Physical Properties

Quantity	A Star	Pre-He WD
a ($R_\odot$)	4.229 ± 0.029	
M ($M_\odot$)	1.430 ± 0.027	0.176 ± 0.004
R ($R_\odot$)	1.46 ± 0.05	0.284 ± 0.003
$\log g$ (cm s^{-2})	4.26 ± 0.04	4.77 ± 0.02
θ (μarcsec)	51.5 ± 1.9	9.98 ± 0.13
$T_{eff}(\theta)$ (K)	8159 ± 135	11636 ± 420
T_{eff}(spectrum) (K)	8048 ± 50	11890 ± 490
$V \sin i$ (km s^{-1})	64.8 ± 1.0	<20
Synchronous $V \sin i$ (km s^{-1})	91	18

6. Component Reconstructed Spectra and Physical Properties

The new *HST*/COS spectra contain a number of features that are important diagnostics of stellar temperature and other physical parameters. Here we examine both the combined and individual spectra (from a Doppler tomography reconstruction) to derive estimates of the effective temperatures and projected rotational velocities and to investigate the properties of the line spectrum of the pre-He WD.
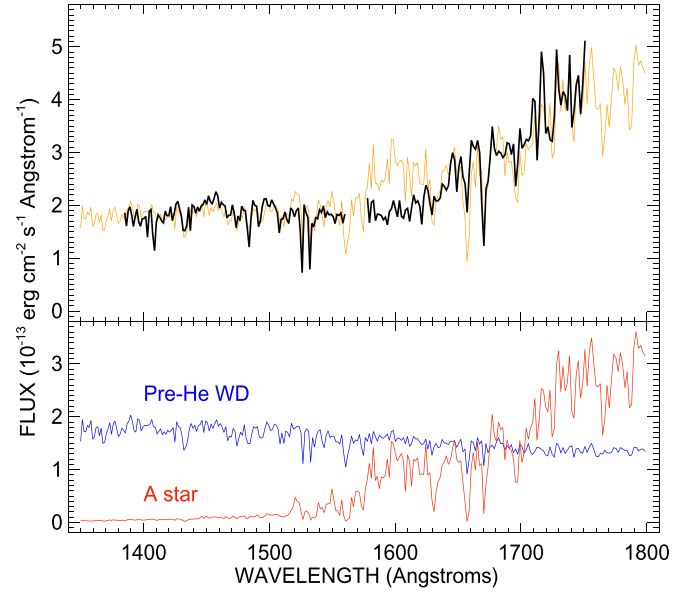

Figure 5. Top panel shows a rebinned, low resolution version of the *HST/COS* spectrum observed on HJD 2457717.5985 (black) with the sum of the model spectra for both components (orange). The bottom panel shows the individual model spectra as described in Section 6 (for metallicities of $[M/H] = 0.0$ and -0.5 for the A star and pre-He WD, respectively).

6.1. Effective Temperatures

We begin by considering the temperatures implied by the absolute fluxes. Figure 5 shows the *HST*/COS spectrum from the first visit together with model spectra for both components (discussed below) rebinned to a lower resolution of $R = 500$. The pre-He WD dominates the flux distribution at the low wavelength end, while the A star becomes stronger beyond 1700 Å. The observed absolute flux f_λ is related to the emitted flux F_λ by

$$f_\lambda = \left(\frac{R}{d}\right)^2 F_\lambda 10^{-0.4A_\lambda} = \frac{1}{4}\theta^2 F_\lambda 10^{-0.4A_\lambda}, \quad (1)$$

where θ is the angular diameter and A_λ is the extinction. In the case at hand, we estimated θ from the physical radii and the distance from Gaia DR2 (Table 4). We adopted the extinction curve from Fitzpatrick (1999) and $E(B - V) = 0.06$ mag and $A_V/E(B - V) = 3.26$ from Gontcharov & Mosenkov (2018) to determine the wavelength-dependent extinction A_λ. Then the observed fluxes can be directly related to the emitted fluxes that

Table 5
$T_{\rm eff}$(spectrum) from Spectral Model Fits

Metallicity [M/H]	$T_{\rm eff}$ [short λ] (K)	χ_ν^2 [short λ]	$T_{\rm eff}$ [long λ] (K)	χ_ν^2 [long λ]
		Pre-He WD		
+0.0	13618 ± 79	1.78	12533 ± 119	2.65
−0.5	12376 ± 88	1.54	11404 ± 68	2.60
−1.0	10800 ± 64	1.75	10112 ± 46	2.71
		A Star		
+0.0	…	…	8048 ± 6	2.91
−0.5	…	…	7730 ± 9	2.27
−1.0	…	…	7424 ± 10	1.95

are primarily dependent on the effective temperature $T_{\rm eff}$. We first created a least-squares fitting procedure that finds the best-fit angular diameters as a function of assumed temperatures based upon model spectra from the UVBLUE grid (Rodríguez-Merino et al. 2005), and then we used this procedure in an iterative scheme to find the temperatures associated with the estimated angular diameters given in Table 4. We adopted model spectra for the gravities listed in Table 4 and for metallicities of $[M/H] = -0.5$ and 0.0 for the pre-He WD and A star, respectively (see below), but the results were relatively insensitive to metallicity. The temperature estimates from the absolute flux and angular diameter are listed as $T_{\rm eff}(\theta)$ in Table 4, and the corresponding model spectral fit is shown in Figure 5. The quoted errors are based upon uncertainties in the *HST*/COS flux calibration, stellar radii, and distance, but the largest factor is the assumed extinction. For example, Maxted et al. (2014) adopted a lower reddening of $E(B - V) = 0.02$, and fits using this reddening led to temperatures that were lower by approximately the errors given for $T_{\rm eff}(\theta)$ in Table 4.

The next estimate of the pre-He WD temperature comes from a comparison of the details of the line spectrum. We reconstructed the individual component spectra of EL CVn using the Doppler tomography technique described by Bagnuolo et al. (1994). This method assigns a radial velocity to each spectrum from the adopted orbital elements (Table 2) and uses initial flux estimates based upon reddened UVBLUE models. The routine then uses an iterative correction scheme to find the individual spectra of the A star and pre-He WD. The tomography algorithm is very sensitive to the details of the line spectra, but less so to the shape of the continuum. Consequently, at the conclusion of the iterations we fit a fourth-order polynomial to the ratio of the high resolution versions of the reconstructed spectra to the model spectra, and then divided by this fit to facilitate a direct comparison of the line features in the reconstructed and model spectra. We repeated this comparison over a grid of temperature values and for the low and high wavelength segments separately, and a best-fit temperature $T_{\rm eff}$(spectrum) was found from the minimum position of the χ_ν^2 residuals between the reconstructed and model spectra. The results of these trials are reported in Table 5. We found that the solar abundance models $[M/H] = 0.0$ predicted lines that were systematically too deep compared to those in the observed spectrum, and this led to a temperature that was much hotter than expected. We subsequently experimented with some of the lower metallicity models in the UVBLUE grid, and the best results in both
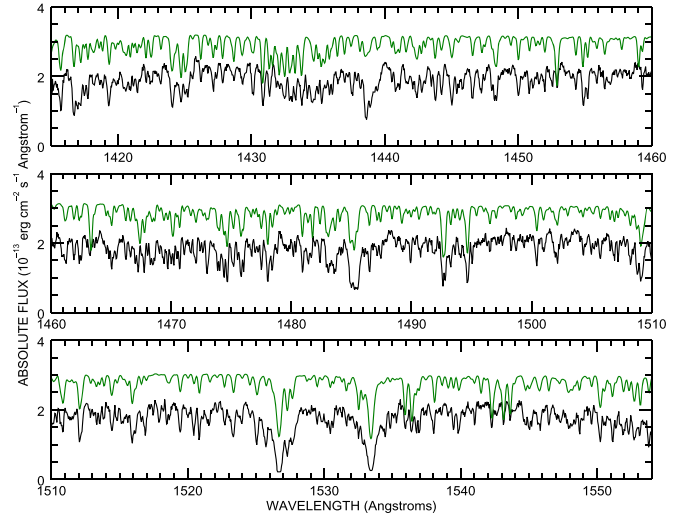

Figure 6. Reconstructed spectrum of the pre-He WD component of EL CVn based upon the *HST*/COS short wavelength data. We plot the absolute flux of the reconstructed pre-He WD spectrum in black and the model spectrum in green ($[M/H] = -0.5$; offset by $+1.0 \times 10^{-13}$).
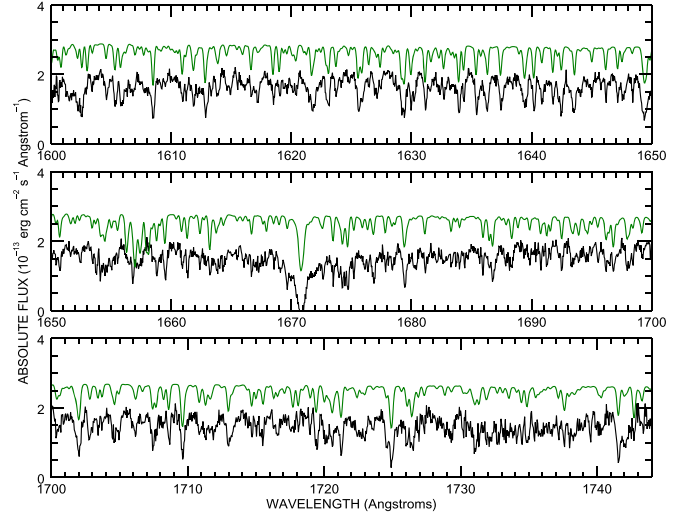

Figure 7. Reconstructed spectrum of the pre-He WD component of EL CVn based upon the *HST*/COS long wavelength data. We plot the absolute flux of the reconstructed pre-He WD spectrum in black and the model spectrum in green ($[M/H] = -0.5$; offset by $+1.0 \times 10^{-13}$).

wavelength segments were obtained with $[M/H] = -0.5$ (Table 5). The average temperature from the fits in both UV segments is listed in Table 4 as $T_{\rm eff}$(spectrum). This estimate of the pre-He WD temperature agrees within errors with both that from the angular diameter method $T_{\rm eff}(\theta)$ and that from the composite fit of the spectral energy distribution made by Maxted et al. (2014) of $T_{\rm eff} = 12{,}000 \pm 900\,{\rm K}$. The reconstructed and model spectra of the pre-He WD for our derived $T_{\rm eff}$(spectrum) are plotted in the panels of Figures 6 and 7.

The absorption line patterns of the A-star spectrum in the *HST*/COS long wavelength segment were harder to match in detail as a temperature diagnostic. However, the shape of the spectral energy distribution and the wavelength where significant flux first appears are very sensitive to the assumed temperature. Consequently, we made comparisons of low resolution versions of the reconstructed and model spectra in the long wavelength segment to explore the variation with
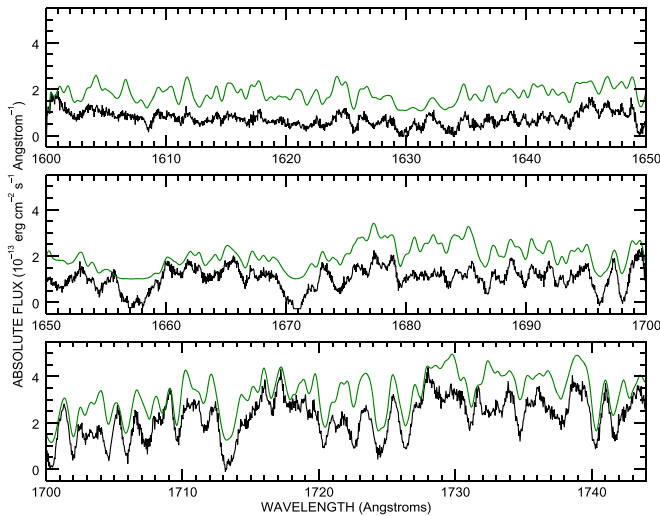
Figure 8. Reconstructed spectrum of the A-star component of EL CVn based upon the *HST*/COS long wavelength data. We plot the absolute flux of the reconstructed A-star spectrum in black and the model spectrum in green ($[M/H] = 0.0$; offset by $+1.0 \times 10^{-13}$).

temperature. The comparison was made over a grid of assumed temperature to find the solution with the lowest χ_ν^2, and these best-fit estimates of $T_{\rm eff}$(spectrum) are given in the lower part of Table 5. Although subsolar metallicity models made better fits, we adopted the solar metallicity temperature for the A star because the lower temperatures associated with lower metallicities yield temperature ratios T_2/T_1 that are inconsistent with fits of the eclipse depths in the LC (Section 4). The derived estimate of $T_{\rm eff}$(spectrum) (Table 4) agrees within errors with estimates from the angular size method and from Maxted et al. (2014) of $T_{\rm eff} = 8250 \pm 350$ K. Figure 8 shows the reconstructed spectra of the A star from the long wavelength segment. The A-star flux was too low and the resulting S/N too small in the short wavelength segment for reliable feature identification.

6.2. Projected Rotational Velocities

We estimated the rotational broadening velocity by creating grids of UVBLUE model spectra convolved with a rotational broadening function for projected rotational velocity $V \sin i$ in the range of 0–110 km s^{-1} with an increment of 5 km s^{-1}. The rotational broadening functions use a linear limb-darkening law (Wade & Rucinski 1985) with wavelength-dependent coefficients based upon the stellar temperature and gravity. The broadened model spectra were compared with the reconstructed FUV spectra to form a distribution of reduced χ_ν^2 as a function of $V \sin i$. The result for the A star is $V \sin i = 64.4 \pm 1.1$ km s^{-1}. On the other hand, the reduced χ_ν^2 of the fits for the pre-He WD spectrum indicated only an upper limit, i.e., the rotational broadening was unresolved in the *HST*/COS spectra.

We also applied the Doppler tomography algorithm to the optical APO/ARCES spectra to reconstruct the spectral components in a few of the echelle orders. The observed and model spectra were rectified through fits of the line-free continuum regions. Once again the radial velocities were taken from the orbital fit, but the flux ratio was fixed according to the radius ratio (Table 4) and the BLUERED model fluxes (Bertone et al. 2008) for the adopted temperatures, gravities, and metallicities. Figure 9 plots the reconstructed spectra in the
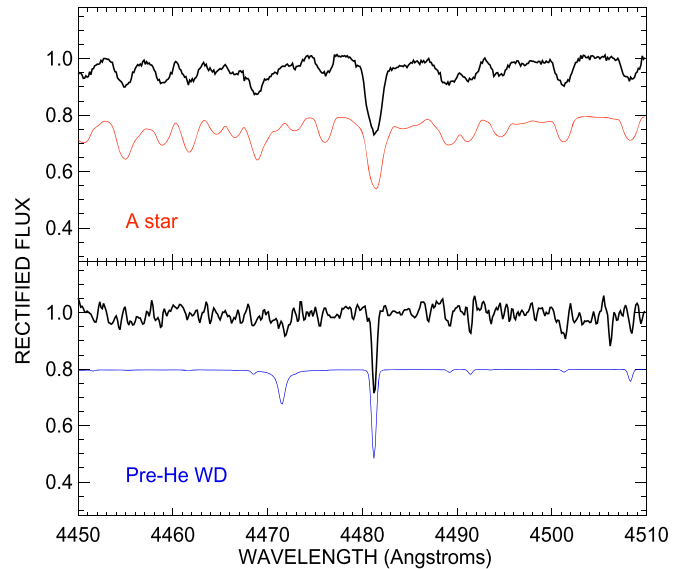

Figure 9. Reconstructed spectra of EL CVn in the vicinity of the Mg II λ4481 line (from APO/ARCES data). The top panel shows the rectified flux of the reconstructed spectrum of the A star in black and the model spectrum in red ($[M/H] = 0.0$; offset by -0.2). The bottom panel displays the reconstructed spectrum of the pre-He WD in black and the model spectrum in blue ($[M/H] = -1.0$; offset by -0.2). Note that the He I λ4471 line predicted in the model is absent from the reconstructed spectrum of the pre-He WD.

vicinity of the Mg II λ4481 feature. We estimated $V \sin i$ for the optical spectra in two regions that contained a number of relatively sharp spectral lines. This was accomplished by forming the CCF of a rotationally broadened model spectrum with a $V \sin i = 0$ model spectrum, and then deriving the relationship between the CCF FWHM and assumed $V \sin i$. Interpolation in this function at the FHWM of the CCF of the reconstructed and zero velocity model spectra led to our estimate of $V \sin i$. We arrived at estimates for the A-type star of $V \sin i = 64.3 \pm 1.8$ km s^{-1} from the Ca I λ4226 region and $V \sin i = 68.1 \pm 2.2$ km s^{-1} from the Mg II λ4481 area. The final average of the *HST*/COS and APO/ARCES measurements is a projected rotational velocity of $V \sin i = 64.8 \pm 1.0$ km s^{-1}. The model A-star spectra shown in Figures 8–11 are based upon this value. Estimates of the predicted synchronous projected rotational velocities are given in the final row of Table 4, and it appears that the A star is rotating at only $\approx 71\%$ of the synchronous rate. This is unusual but not unprecedented among short-period binaries (Lurie et al. 2017).

6.3. Pre-He WD Features in the Optical Spectrum

Our initial inspection of APO/ARCES spectra revealed only a single feature, Mg II λ4481, that could be reliably associated with the pre-He WD. Nevertheless, we used the Doppler tomography reconstructed spectra to search for other pre-He WD lines in the echelle orders recording Mg II λ4481, Hβ λ4861, and Hα λ6563. We adopted flux ratios using radii and model surface fluxes (for $T_{\rm eff}$(spectrum)) based on the results in Table 4 ($f_2/f_1 = 0.11$, 0.10, and 0.08 for the three feature wavelengths, respectively). The reconstructed spectra show a low frequency variation in the continuum placement, and we relied upon forming ratios with the model spectra to rectify the reconstructed spectra for comparison purposes. The reconstructed optical spectra and corresponding models are shown in Figures 9–11, and we were gratified that this process revealed
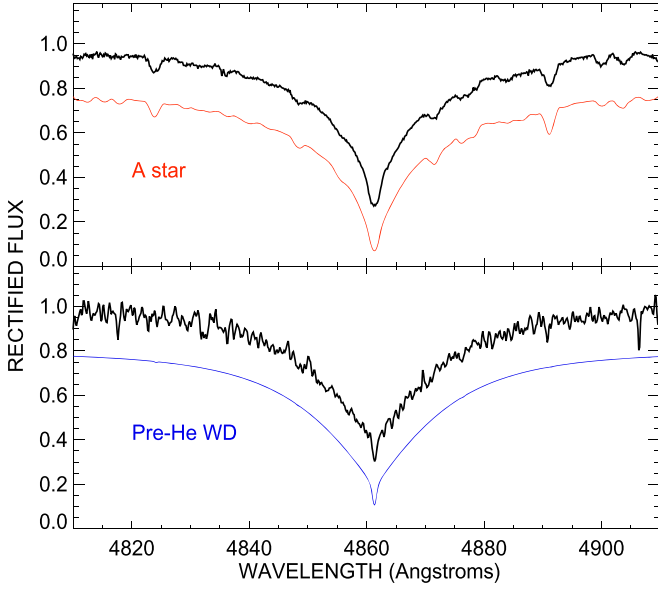
Figure 10. Reconstructed spectra of EL CVn in the vicinity of Hβ (from APO/ARCES data). The top panel shows the rectified flux of the reconstructed spectrum of the A star in black and the model spectrum in red ($[M/H] = 0.0$; offset by -0.2). The bottom panel displays the reconstructed spectrum of the pre-He WD in black and the model spectrum in blue ($[M/H] = -1.0$; offset by -0.2).
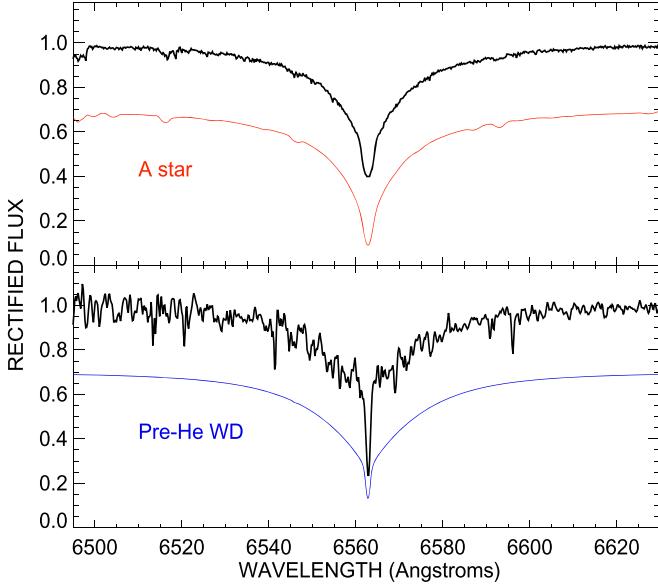

Figure 11. Reconstructed spectra of EL CVn in the vicinity of Hα (from APO/ARCES data). The top panel shows the rectified flux of the reconstructed spectrum of the A star in black and the model spectrum in red ($[M/H] = 0.0$; offset by -0.3). The bottom panel displays the reconstructed spectrum of the pre-He WD in black and the model spectrum in blue ($[M/H] = -1.0$; offset by -0.3).

the presence of the Hβ and Hα lines of the pre-He WD. The Hα feature of the pre-He WD shows a narrow core that is often observed in DA WDs and results from non-LTE effects in the upper atmosphere (Koester & Herrero 1988) that are not treated in the LTE models we used.

7. Evolutionary State of EL CVn

Chen et al. (2017) investigated the formation of EL CVn-type binaries using evolutionary tracks from the Modules for
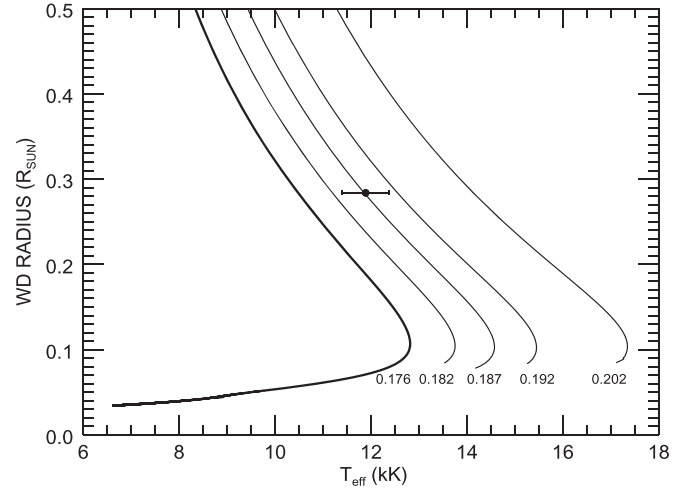

Figure 12. Evolutionary tracks of pre-He WD stars from Althaus et al. (2013) in the (T_{eff}, R) plane for several assumed masses (labeled in units of $M_\odot$). The thick line shows the track for the mass determined for the pre-He WD ($0.176 \pm 0.009\,M_\odot$). We plot the measured T_{eff}, R of the pre-He WD component (Sections 5, 6) as an open circle with the associated uncertainties, and these show that the star is overluminous for its mass.

Experiments in Stellar Astrophysics (MESA). They assume that these systems are Population I binaries that experienced non-conservative, stable mass transfer when the mass donor entered the red giant stage. They find that the most common pre-He WDs have masses within 0.17–0.21 $M_\odot$ and have companions in the mass range of $1.3-1.5\,M_\odot$. The components of EL CVn have masses that fall within these ranges. Mass transfer during the red giant stage will depend on the radius of the envelope and thus on the core mass. Models by Lin et al. (2011), Istrate et al. (2016), and others predict that following envelope loss, there will be a close relationship between the mass of the remnant core and the orbital period. The fact that the pre-He WD mass and orbital period of EL CVn agree well with these predictions (e.g., Figure 19 in Istrate et al. 2016 and Figure 6 in van Roestel et al. 2018) offers indirect evidence that it formed through mass transfer during the red giant stage of the progenitor.

Following the completion of mass transfer, the stripped cores may have a thick hydrogen envelope that can continue to power nuclear burning. Althaus et al. (2013) used the stellar evolutionary code LPCODE to generate evolutionary tracks of extremely low-mass WDs with He cores in the mass range of $0.15-0.45\,M_\odot$. They show that the stars may experience intermittent H-burning as CNO shell flashes that will change their evolutionary trajectory in the (T_{eff}, g) plane. van Roestel et al. (2018) compared these evolutionary sequences to the properties of 36 EL CVn-type binaries discovered through the Palomar Transient Factory, and the observationally determined masses and temperatures are in broad agreement with the models. Similar evolutionary sequences of extremely low-mass WDs were investigated by Calcaferro et al. (2018), who focused on remnants with thinner H envelopes. They find that a thinner envelope yields remnants with higher gravities and shorter cooling times. The derived gravity of the pre-He WD in EL CVn is much lower than found from their calculations, so instead the pre-He WD in EL CVn probably has a thick H envelope as suggested by Maxted et al. (2014).

In Figure 12, we show the evolutionary sequences from Althaus et al. (2013) in the (T_{eff}, R) plane for several assumed

masses. We also plot these parameters for the pre-He WD in EL CVn. We see that the observed temperature and radius correspond to a mass track for an object of $0.187\,M_{\odot}$ or about 6% (3σ) more massive than we find. This suggests that the pre-He WD is somewhat overluminous for its mass in the context of these evolutionary tracks. Istrate et al. (2016) calculated similar cooling tracks for several assumptions about atmospheric elemental diffusion and rotational mixing, and their tracks have cooler temperatures than those of Althaus et al. (2013) for masses below $0.2\,M_{\odot}$. The observed (T_{eff}, R) of the pre-He WD corresponds to a mass of $0.199\,M_{\odot}$ in the $Z = 0.02$, diffusion plus rotation models of Istrate et al. (2016), indicating an even greater overluminosity with respect to these models.

The evolutionary models indicate that a relatively long time span has elapsed since the conclusion of Roche-lobe overflow, and this means that the pre-He WD has had sufficient time for elemental diffusion processes to occur (Istrate et al. 2016). We found that the metal lines of the pre-He WD indicate a subsolar metallicity that could be the result of such processes. Furthermore, an inspection of the *HST*/COS reconstructed spectrum of the pre-He WD indicates a number of differences from the predictions of the UVBLUE model for a metallicity of $[M/H] = -0.5$. Several lines are much stronger than predicted (Si II $\lambda\lambda1526.7$, 1533.4; Al II $\lambda1670.8$), while others are weaker or absent (P II $\lambda\lambda1542.9$, 1535.9, 1536.4, 1542.3, 1543.1, 1543.6; C I $\lambda\lambda1459.0$, 1463.3, 1467.4, 1470.1, 1481.8, 1656.3, 1657.0, 1657.9). Only Mg II $\lambda4481$ is readily visible in the optical spectrum, and we found that it is also weaker than expected for solar metallicity. The best match from the BLUERED grid was made with $[M/H] = -1.0$ (Figure 9). Note that for our derived pre-He WD temperature, the model predicts that He I $\lambda4471$ should be present in the spectrum, but in the reconstructed spectrum it appears to be absent (Figure 9). This suggests that the atmosphere is depleted in He. These differences are probably related to elemental diffusion processes in the pre-He WD atmosphere that will cause hydrogen to rise and heavier elements to sink. Istrate et al. (2016) discuss how the outcome of these processes depend on the competition between gravitational settling and rotational mixing. Their diffusion model for a $0.176\,M_{\odot}$ star indicates that He and C will have settled out of the atmosphere by 300 Myr after envelope stripping, much less than present cooling age of 570 Myr based upon their evolutionary tracks for the observed radius. These clues from spectroscopy suggest that the atmosphere of EL CVn is enriched in hydrogen and depleted in most heavier elements as predicted by evolutionary models.

8. Conclusions

EL CVn is the prototype of post-mass transfer binaries in which the stripped mass donor star has not yet contracted to WD dimensions, and, given a favorable orientation, such objects can be detected as eclipsing binaries with extremely fast ingress and egress durations. Determing the physical properties of the hot remnant star requires spectroscopic analysis in the UV part of the spectrum where their flux dominates. This *HST*/COS study of EL CVn demonstrates the scientific rewards of high resolution spectroscopy in the wavelength domain where the spectrum of the hot remnant shines clearly.

Our first task was to identify the spectral lines of the hot pre-He WD and to use their orbital Doppler shifts to find the mass ratio. The *HST*/COS spectra revealed metallic lines in the FUV

and the APO/ARCES spectra showed the presence of the Mg II $\lambda4481$ line associated with the pre-He WD. By combining radial velocity measurements for both stars with a reconsideration of the eclipse LC, we find that the masses of the components are $1.430 \pm 0.027\,M_{\odot}$ and $0.176 \pm 0.004\,M_{\odot}$ for the A star and pre-He WD, respectively. Analysis of the LC yields the corresponding radii of 1.46 ± 0.05 and $0.284 \pm 0.003\,R_{\odot}$.

We applied three methods to estimate the effective temperatures. The absolute fluxes of the stars depend on their temperatures, angular sizes, and interstellar extinction, and by setting the angular size from the physical radii and distance from Gaia DR2 we were able to infer the temperatures of both components. We obtained additional temperature estimates by comparing the observed and model line strengths of the pre-He WD and the flux distribution of the A star. The results agree within errors and lead to model eclipse depths that match the observed LC: $T_{\text{eff}} = 8100 \pm 100\,\text{K}$ and $11,800 \pm 400\,\text{K}$ for the A star and pre-He WD, respectively. We caution, however, that these results rely on model atmospheres for standard abundance distributions that may not be appropriate for the pre-He WD star.

The mass gainer star has a mass and radius like that of an F-type MS star, but has a temperature associated with a mid-A-type star of solar metallicity (Pecaut & Mamajek 2013). For example, the MESA Isochrones & Stellar Tracks code (Choi et al. 2016; Dotter 2016) predicts a maximum MS temperature of 7065 K for a $1.43\,M_{\odot}$ star with solar metallicity, and the hotter temperature we find would only be consistent with a subsolar metallicity. The probable overluminosity for its mass may be a consequence of mixing of new nuclear fuel from mass accretion during the mass transfer stage.

The properties of the hot pre-He WD star agree in many ways with the predictions of model evolutionary sequences. The star's mass and orbital period place it precisely on the (M, P) relation expected for stars that were stripped of their envelopes during the red giant stage. However, the star is slightly hotter than expected for its mass and radius relative to the evolutionary tracks from Althaus et al. (2013) and Istrate et al. (2016). The metallic line spectrum in the FUV is suggestive of a subsolar metallicity that is unexpected given the relative youth implied by the total system mass and its thin disk kinematics (Maxted et al. 2014). We suggest that the low metal abundances are rather the result of elemental diffusion processes in the outer envelope that play a major role in setting the chemistry of WD atmospheres (Koester & Chanmugam 1990). Diffusion will cause H to float upwards and heavier elements to sink, and indeed the optical spectra show that the H-Balmer lines are strong while He lines are weak or absent. Furthermore, we find that not all the heavier elements are reduced in similar proportions. For example, the ultraviolet spectra indicate that the C and P lines are very weak while the Si and Al lines are relatively stronger. The chemistry of the atmosphere of the hot pre-He WD star offers us a key insight into the processes that lead eventually to the striking abundance differences among the WD stars.

Wang et al.

Facilities: HST (COS), ARC (ARCES), ING:*Herschel* (pt5m).

Software: ATLAS9 (Castelli & Kurucz 2003), SYNTHE (Rodríguez-Merino et al. 2005), Eclipsing Light Curve code (Orosz & Hauschildt 2000), ULTRACAM pipeline software (Dhillon et al. 2007), IRAF (Tody 1986, 1993), COS pipeline (Fischer 2019), MIST (Choi et al. 2016; Dotter 2016).

ORCID iDs

Luqian Wang (王璐茜) ⓘ https://orcid.org/0000-0003-4511-6800
Douglas R. Gies ⓘ https://orcid.org/0000-0001-8537-3583
Kathryn V. Lester ⓘ https://orcid.org/0000-0002-9903-9911
Zhao Guo ⓘ https://orcid.org/0000-0002-0951-2171
Rachel A. Matson ⓘ https://orcid.org/0000-0001-7233-7508
Stuart P. Littlefair ⓘ https://orcid.org/0000-0001-7221-855X
Pierre F. L. Maxted ⓘ https://orcid.org/0000-0003-3794-1317

References

Althaus, L. G., Miller Bertolami, M. M., & Córsico, A. H. 2013, A&A, 557, A19
Bagnuolo, W. G., Jr., Gies, D. R., Hahula, M. E., Wiemker, R., & Wiggs, M. S. 1994, ApJ, 423, 446
Bailer-Jones, C. A. L., Rybizki, J., Fouesneau, M., Mantelet, G., & Andrae, R. 2018, AJ, 156, 58
Bertone, E., Buzzoni, A., Chávez, M., & Rodríguez-Merino, L. H. 2008, A&A, 485, 823
Bloemen, S., Marsh, T. R., Degroote, P., et al. 2012, MNRAS, 422, 2600
Breton, R. P., Rappaport, S. A., van Kerkwijk, M. H., & Carter, J. A. 2012, ApJ, 748, 115
Calcaferro, L. M., Althaus, L. G., & Córsico, A. H. 2018, A&A, 614, A49
Carter, J. A., Rappaport, S., & Fabrycky, D. 2011, ApJ, 728, 139
Castelli, F., & Kurucz, R. L. 2003, in IAU Symp. 210, Modelling of Stellar Atmospheres, ed. N. Piskunov, W. W. Weiss, & D. F. Gray (Tucson, AZ: Univ. Arizona Press), A20
Chen, X., Maxted, P. F. L., Li, J., & Han, Z. 2017, MNRAS, 467, 1874
Choi, J., Dotter, A., Conroy, C., et al. 2016, ApJ, 823, 102
Danforth, C. W., Keeney, B. A., Stocke, J. T., Shull, J. M., & Yao, Y. 2010, ApJ, 720, 976
Dhillon, V. S., Marsh, T. R., Stevenson, M. J., et al. 2007, MNRAS, 378, 825
Dotter, A. 2016, ApJS, 222, 8
Faigler, S., Kull, I., Mazeh, T., et al. 2015, ApJ, 815, 26
Fischer, W. J., et al. 2019, Cosmic Origins Spectrograph Instrument Handbook, Version 11.0 (Baltimore, MD: STScI)
Fitzpatrick, E. L. 1999, PASP, 111, 63
Gontcharov, G. A., & Mosenkov, A. V. 2018, MNRAS, 475, 1121
Green, J. C., Froning, C. S., Osterman, S., et al. 2012, ApJ, 744, 60
Guo, Z., Gies, D. R., Matson, R. A., et al. 2017, ApJ, 837, 114
Hardy, L. K., Butterley, T., Dhillon, V. S., Littlefair, S. P., & Wilson, R. W. 2015, MNRAS, 454, 4316
Istrate, A. G., Marchant, P., Tauris, T. M., et al. 2016, A&A, 595, A35
Koester, D., & Chanmugam, G. 1990, RPPh, 53, 837
Koester, D., & Herrero, A. 1988, ApJ, 332, 910
Kolbas, V., Pavlovski, K., Southworth, J., et al. 2015, MNRAS, 451, 4150
Lin, J., Rappaport, S., Podsiadlowski, P., et al. 2011, ApJ, 732, 70
Lurie, J. C., Vyhmeister, K., Hawley, S. L., et al. 2017, AJ, 154, 250
Masuda, K., Kawahara, H., Latham, D. W., et al. 2019, ApJL, 881, L3
Matson, R. A., Gies, D. R., Guo, Z., et al. 2015, ApJ, 806, 155
Matson, R. A., Gies, D. R., Guo, Z., & Orosz, J. A. 2016, AJ, 151, 139
Maxted, P. F. L., Anderson, D. R., Burleigh, M. R., et al. 2011, MNRAS, 418, 1156
Maxted, P. F. L., Bloemen, S., Heber, U., et al. 2014, MNRAS, 437, 1681
Morbey, C. L., & Brosterhus, E. B. 1974, PASP, 86, 455
Orosz, J. A., & Hauschildt, P. H. 2000, A&A, 364, 265
Otero, S. A., & Dubovsky, P. A. 2004, IBVS, 5557, 1
Pecaut, M. J., & Mamajek, E. E. 2013, ApJS, 208, 9
Rappaport, S., Nelson, L., Levine, A., et al. 2015, ApJ, 803, 82
Rodríguez-Merino, L. H., Chavez, M., Bertone, E., & Buzzoni, A. 2005, ApJ, 626, 411
Tody, D. 1986, Proc. SPIE, 627, 733
Tody, D. 1993, in ASP Conf. Ser. 52, Astronomical Data Analysis Software and Systems II, ed. R. J. Hanisch, R. J. V. Brissenden, & J. Barnes (San Francisco, CA: ASP), 173
van Kerkwijk, M. H., Rappaport, S. A., Breton, R. P., et al. 2010, ApJ, 715, 51
van Roestel, J., Kupfer, T., Ruiz-Carmona, R., et al. 2018, MNRAS, 475, 2560
Wade, R. A., & Rucinski, S. M. 1985, A&AS, 60, 471
Wang, K., Luo, C., Zhang, X., et al. 2018, AJ, 156, 187
Wang, L., Gies, D. R., & Peters, G. J. 2017, ApJ, 843, 60
Wang, S.-i., Hildebrand, R. H., Hobbs, L. M., et al. 2003, Proc. SPIE, 4841, 1145
Zhang, X. B., Fu, J. N., Liu, N., Luo, C. Q., & Ren, A. B. 2017, ApJ, 850, 125
Zucker, S. 2003, MNRAS, 342, 1291